

Time-variable strain and stress rates induced by Holocene glacial isostatic adjustment in continental interiors

T.J. Craig

COMET, School of Earth and Environment, The University of Leeds,
Leeds, United Kingdom. LS2 9JT

Corresponding author: t.j.craig@leeds.ac.uk

E. Calais

École normale supérieure, Department of Geosciences, Université PSL, 24 rue Lhomond,
75231 Paris, France.

Université Côte d'Azur, CNRS, IRD, Observatoire de la Côte d'Azur, Géoazur, France.

L. Fleitout

École normale supérieure, Department of Geosciences, Université PSL, 24 rue Lhomond,
75231 Paris, France.

L. Bollinger

CEA, DAM, DIF, 91297 Arpajon, France.

O. Scotti

IRSN/PRP-DGE/SCCAN/BERSSIN, 92262 Fontenay-aux-Roses, France.

This submission is a non-peer reviewed preprint, available via EarthArXiv

1 Time-variable Strain and Stress Rates Induced by Holocene
2 Glacial Isostatic Adjustment in Continental Interiors

3 T.J. Craig¹, E. Calais^{2,3}, L. Fleitout², L. Bollinger⁴, and O. Scotti⁵

4 ¹*COMET, Institute of Geophysics and Tectonics, School of Earth and Environment, University of*
5 *Leeds, Leeds, LS2 9JT, UK*

6 ²*École normale supérieure, Department of Geosciences, Université PSL, 24 rue Lhomond, 75231*
7 *Paris, France*

8 ³*Université Côte d'Azur, CNRS, IRD, Observatoire de la Côte d'Azur, Géoazur, France*

9 ⁴*CEA, DAM, DIF, 91297 Arpajon, France*

10 ⁵*IRSN/PRP-DGE/SCAN/BERSSIN, 92262 Fontenay-aux-Roses, France*

11 **Abstract**

12 **Keywords:** Postglacial deformation, intraplate deformation, continental seismicity,
13 strain-rates.

14
15 In continental interiors, tectonically-driven deformation rates are low, often to the point
16 where they are undetectable with modern geodesy. However, a range of non-tectonic sur-
17 face processes, particularly relating to hydrological, cryospheric, and sedimentological mass
18 changes, can produce strain-rates which on geologically-short timescales are substantially
19 greater than those produced by tectonics. Here, we illustrate the problem that such tran-
20 sient strain rates may pose in low-strain environments by considering the impact that the
21 growth and decay of the Fennoscandian and Laurentian ice sheets over the Holocene had
22 on Europe and North America respectively. Induced deformation extended far beyond the

periphery of the ice sheets, with the potential to impact on seismicity rates thousands of kilometres south of the maximum ice extent. We consider how the modelled non-tectonic deformation would have interacted with several known active fault systems, including the European Cenozoic Rift System and the New Madrid fault system. In low strain continental interiors, seismic hazard assessment – crucial for the long-term planning of critical infrastructure, including nuclear waste disposal – is often dependent on sparse information from observational and historical seismicity, and from paleoseismological studies of surface fault systems. We recommend that for a more complete seismic hazard assessment, the impact of non-tectonic transients should be considered – both in the context of the role such transients may have played in recent seismicity, and the role they may play in seismicity to come. Whilst such consideration has previously been given to the direct impact on glacial loading in areas directly glaciated, we show that it should also be considered much more broadly.

1 Introduction

The sparse distribution and often clustered occurrence of large earthquakes in slowly-deforming plate interiors challenges our understanding of the underlying causes of such seismicity, and hampers efforts to reliably determine the seismic hazard in these areas [e.g., Camelbeeck et al., 2007, Calais and Stein, 2009, Hough and Page, 2011, Liu and Stein, 2016, Calais et al., 2016]. Modern space geodesy remains unable to detect the localised build up of elastic strain around faults in continental interiors, even in areas where large earthquakes have repeatedly occurred [e.g., Craig and Calais, 2014, Boyd et al., 2015]. As a result, seismic hazard assessment for such areas relies on historical and instrumental seismicity catalogues and, where available, paleoseismic studies of active fault systems. However, in such slowly-deforming regions, seismicity catalogs only capture a short-duration time interval of the fault activity, and are unlikely to be representative of their longer-term seismogenic potential [e.g., Stein et al., 2012].

48 In addition, the usual assumption that paleo-earthquakes, when they can be identified and
49 characterised, occurred under strain rates that are equivalent to the present-day ones – and are
50 therefore relevant guidelines for short-term hazard assessment – may not be valid [Craig et al.,
51 2016]. Indeed, contrary to plate boundary settings where interseismic strain rates are largely
52 dominated by tectonic loading, strain rates in plate interiors can be significantly affected by
53 transient non-tectonic processes that overwhelm the very slow – if any – tectonic loading.
54 Examples abound of changes in surface or near-surface loading that result in measurable
55 deformation of the lithosphere, with the potential to influence seismicity [e.g. Muir-Wood,
56 1989, Heki, 2003, Mazzotti et al., 2005, Luttrell et al., 2007, Bettinelli et al., 2007, Lagerbäck
57 and Sundh, 2008, Calais et al., 2010, Amos et al., 2014, Craig et al., 2016, 2017, Johnson
58 et al., 2017]. Such load changes can result from a number of causes acting over a range
59 of timescales, from the annual and sub-annual variation of seasonal hydrological loads, to
60 the kyr-timescales of ice sheet variations, or to the Myr-timescales of large-scale sediment
61 removal and redistribution. Similarly, they can operate at a variety of spatial scales, from the
62 relatively localised deformation that results from the anthropogenic removal of groundwater,
63 or the modulation of local surface loads caused by the volume change of major lakes, to the
64 continental scale of major ice sheets, or the global effect of changing ocean volumes.

65 Whilst at plate boundaries, and in regions of relatively rapid tectonic deformation, the
66 rates of deformation induced by such surficial processes are typically swamped by the underly-
67 ing tectonically-driven deformation, in slowly deforming plate interiors the deformation rates
68 driven by surface processes may in contrast be far greater than any underlying tectonic signal.
69 This can result in a strain-rate field that is dominated by short-term transients, and may not,
70 at any given point in time, be representative of the underlying stress or strain state of the
71 crust, or of the longer-term trend in strain accumulation. A classic example is the dominant
72 influence of post-glacial rebound in the present-day geodetic strain-rate field of tectonically-

73 stable central-eastern North America and Fennoscandia [Nocquet et al., 2005, Calais et al.,
74 2006, Kierulf et al., 2014, Kreemer et al., 2014, 2018]. In areas where such a non-tectonic
75 overprint is present – or has been present over the timescales used in paleoseismological stud-
76 ies – one must be cautious equating strain release by paleoearthquakes to present-day strain
77 (or stressing) rates on faults. The extreme case for this is in Fennoscandia, where the crust
78 overlain by major icesheet thicknesses during the LGM is well-established to have hosted a
79 number of major active faults and inferred earthquakes over the 10 ka since the last decay of
80 the icesheet [e.g., Muir-Wood, 1989, Wu et al., 1999, Lagerbäck and Sundh, 2008, Craig et al.,
81 2016, Ojala et al., 2019].

82 Much of continental Europe, with the exception of the Alpine orogenic belt and the Balkans,
83 is commonly regarded as a stable continental interior, characterised by low levels of seismic
84 activity. Geodetically observable strain accumulation related to ongoing tectonic deformation
85 is yet to be conclusively detected [Nocquet, 2012], but is likely to be $< 1 \times 10^{-9} \text{ yr}^{-1}$ across
86 the continental interior. However, major earthquakes have occurred sporadically (e.g., Basel,
87 1356; Dover Strait, 1580; Düren, 1756; Lisbon, 1755), and there is widespread but sparse
88 low-level instrumental seismicity across the continent from the British Isles to Karelia, and
89 paleoseismological works suggest several areas of active deformation (e.g., along the Rhine
90 Graben [e.g., Camelbeeck et al., 2007, Grützner et al., 2016, Van Balen et al., 2019], Lower
91 Saxony Basin [e.g., Brandes et al., 2012, Brandes and Winsemann, 2013, Brandes et al., 2018],
92 Cheb Basin [e.g., Štěpančíková et al., 2019], and the Sudetic Marginal Front [e.g., Štěpančíková
93 et al., 2012, 2022]).

94 Similarly, North America, east of the Rocky Mountains and Cascades, is considered as
95 a stable continental interior, largely seismically quiescent. However, there are a few notable
96 areas of localized seismicity (e.g., the New Madrid Seismic Zone, the East Tennessee Seismic
97 Zone, the St. Lawrence Valley Seismic Zone), although none of these have detectable ongoing

98 tectonic strain accumulation associated with them [Craig and Calais, 2014, Kreemer et al.,
99 2014, Boyd et al., 2015, Kreemer et al., 2018].

100 In this work, we seek to quantify the time-dependent strain and stress rates in continental
101 interiors associated with the evolution of the volume of the major northern hemisphere ice
102 sheets, and how this may impact fault activation in Europe and North America. Our calcula-
103 tions focus on the European ice sheets (principally those over Fennoscandia, the Alps and the
104 British Isles - see Figure 1a) over ~ 40 ka, and the Laurentian icesheet of North America (see
105 Figure 3a).

106 Several studies have indeed suggested that the distal effects of the Fennoscandian deglacia-
107 tion influenced fault behaviour of central Europe in the Holocene – Late Pleistocene. Houtgast
108 et al. [2005] used variations in sedimentation rate across the Geleen Fault (Netherlands) to
109 infer an increased slip-rate between 10 and 15 ka that they relate to glacially-induced vari-
110 ations in the regional deformation rate. In northern Germany, the reactivation of faults in
111 the Lower Saxony Basin, interpreted from the deformation of Pleistocene sediments, has been
112 suggested to result from the development and decay of the Fennoscandian forebulge [Brandes
113 et al., 2012, Brandes and Winsemann, 2013, Brandes et al., 2015].

114 In North America, fewer studies have considered the interaction of ice sheets on fault
115 systems, but examples include New Madrid [Grollmund and Zoback, 2001], the Teton Ranges
116 and Basin and Range [e.g., Hampel et al., 2007] and Alaska [Sauber and Molnia, 2004, Sauber
117 and Ruppert, 2008].

118 Here we will show that the far-field strain-rates resulting from changes in the ice load
119 have been significantly greater in the past 25 Ka than the slow rates of tectonic deformation
120 currently taking place in continental Europe, and that they have migrated significantly over
121 time. Whilst the mode of failure in earthquakes reflects the release of long-term tectonic
122 stresses, and not the transient stresses induced by changing surface loads, their timing and

123 location may be affected by these transients. Although the models presented here are non-
124 unique, they provide quantitative estimates of strain and stress rate variations that should
125 help in interpreting paleoseismic records for seismic hazard assessment without more detailed
126 consideration of the role of non-tectonic processes. This is particularly important for critical
127 infrastructure – nuclear waste storage and disposal facilities, for instance – whose design is
128 based on safety projections over very long time intervals (10^3 to 10^6 years), and which are
129 typically sited in low-strain environments.

130 **2 Modelling Approach**

131 To assess the effect of the redistribution of ice masses on continental strain rates in Europe,
132 we construct a series of models that allow us to calculate stress and strain that result from
133 changes in surface loading over a glacial cycle, similar to the approach described in Craig et al.
134 [2016] and Caron et al. [2017]. Models are constructed under the assumption that the Earth
135 behaves as a self-gravitating visco-elastic sphere (radius 6371 km). We calculate the response
136 of the crust and mantle to a periodic surface load, expressed up to a spatial resolution of
137 spherical harmonic coefficient 128, equating to a lateral resolution of ~ 300 km at the Earth's
138 surface. Boundary conditions are specified at the core-mantle boundary (2891 km depth) and
139 at the free surface, where changes in surface load are applied as a pre-determined time-variable
140 radial stress.

141 Unlike commonly used methods based on the computation of normal modes, our method
142 is based on the Fourier decomposition of the time-dependent variation for each spherical har-
143 monic component of the load. The response of the Earth for each spherical harmonic and each
144 time-frequency is then computed using the classical method used for computing elastic Love
145 numbers [Alterman et al., 1959, Cathles, 1975] except that the elastic parameters are replaced
146 by complex numbers which represent the viscoelastic parameters function of the frequency.

147 We use the ANU-ICE model for changes in the extent and volume of major ice sheets
148 through time. This ice model and our modelling approach are global in extent. We resampled
149 the initial ice model onto a $1^\circ \times 1^\circ$ spatial grid and to 1 ka time intervals, by linear interpolation.
150 ANU-ICE covers multiple glacial cycles, extending back to 250 ka. Since our modelling ap-
151 proach requires, for mathematical simplicity, that the surface load variation over the timescale
152 of the model be periodic, this 250 ka loading cycle is supplemented by an additional 200 ka of
153 no load change from the present, in order to allow for relaxation of the glacial process. Then
154 the loading cycles are merged back into the the re-initialisation of glaciation at 250 ka to create
155 a periodic signal.

156 Accumulation of the Fennoscandian ice sheet takes place over the late Pleistocene to the
157 last glacial maximum at 23-20 ka. Then ice retreat takes place gradually until 10 ka, at
158 which point deglaciation of Fennoscandia is complete. In the British Isles, ice is concentrated
159 over Scotland and areas of northern England, northern Ireland and Wales. It is connected to
160 the main Fennoscandian ice sheet during peak glaciation, but with both the peak and final
161 termination of major glaciation occurring slightly earlier, at ~ 25 ka and ~ 15 ka respectively.
162 The Alpine ice sheet, whilst much more minor in amplitude and extent than the previous two,
163 is important for strain patterns in central Europe. It peaked between ~ 24 and ~ 10 ka, with
164 a relatively rapid decline accomplished by ~ 7 ka. In North America, the Laurentian ice sheet
165 covered much of Canada and the northmost USA over the Pleistocene, peaking at ~ 20 ka,
166 before a more gradual, steady decline and retreat until end glaciation at around ~ 6 ka.

167 The ice loading model is adapted to account for the conjugate changes in oceanic load-
168 ing. At the resolution of our model, fully solving the sea-level equation would produce only
169 minor variations in the strain and stress fields. We instead implement broad-scale changes in
170 oceanic loading by redistributing uniformly across the oceans the ice load removed without
171 modifying coastlines, whilst conserving the total equivalent water load at all times steps. We

172 do not recalculate coastlines at each time interval, and so exclude from our model the flooding
173 of shallow continental shelf regions regions like Irish Sea, North Sea, English Channel, and
174 northernmost Adriatic and the effect this would have on the near-field stress and strain fields.
175 The exception to this is the loading of the Black Sea, which we model as being unconnected to
176 the global oceanic system prior to 7 ka. At 7 ka, the opening of the Bosphorus Strait leads to
177 the integration of the Black Sea back into the global oceanic system. This only has a secondary
178 effect (compared to global sea-level changes) on the strain and stress fields of Anatolia around
179 7 ka.

180 The flooding of the Black Sea produces a notable kink in the strain-rate profile for Anatolia,
181 as shown on Figure 2 at 7 ka, and has been suggested to play a major role in the stress state
182 of Anatolia, particularly around the North Anatolian Fault [Luttrell et al., 2007]. However,
183 given the relatively small contribution of the Black Sea to the total oceanic volume, this
184 has minimal effects on more distal regions, with no discernible associated kink in strain rate
185 present in profiles on Figure 2 at greater distances from the Black Sea. Hence, whilst the
186 precise timing and rate of this Black Sea flooding remains a topic of some debate [Ryan et al.,
187 2003], variations of a few kas do not significantly alter our model results. For simplicity, shallow
188 endorheic oceans such as the Caspian Sea, Lake Chad, etc. are assumed to be disconnected
189 from the global ice/ocean system, and their load-evolution is not incorporated into our model.

190 Elastic properties are taken from the seismologically-derived one-dimensional Preliminary
191 Reference Earth Model [Dziewonski and Anderson, 1981] for a spherically-symmetric Earth.
192 The 1-dimensional viscosity (η) structure used is based on that of Zhao et al. [2012], which
193 comes twinned with the ANU-ICE model which we are also using. It incorporates a 101 km-
194 thick elastic lithosphere over an upper mantle with $\eta = 4.2 \times 10^{20}$ Pa s, a lower mantle with
195 $\eta = 1.0 \times 10^{21}$ Pa s, and a transition between the two at 660 km below the free surface.
196 Comparisons to models constructed using the same approach from the ICE-5G ice history

197 model [Peltier, 2004] and the twinned VM5a viscosity structure [Peltier and Drummond, 2008]
198 demonstrate that, whilst the finer details of the strain and stress field generated do differ, the
199 large-scale features which are the concern of this paper are found in both Earth/ice model
200 pairs. These small-scale differences are smaller than other unquantified effects such as that
201 of failing to incorporate the 3-dimensional structure of both the elastic lithosphere and the
202 visco-elastic underlying mantle.

203 The most problematic issue in such calculations results from the relatively under-constrained
204 viscosity of the lower mantle. Observational constraints on the viscosity of the lower mantle
205 are largely derived from long-wavelength GIA, and viscosity is determined in conjunction with
206 long-wavelength ice load history [e.g., Peltier, 2004, Zhao et al., 2012]. For the Laurentian
207 icesheet in North America, this poses a particular problem, due to the sheer scale of the ice
208 sheet at its maximum extent, and the paucity of geological and geomorphological data from the
209 continental interior to constrain this. Here, where we are mainly concerned with the far-field
210 effects of ice-loading beyond the edges of the ice margin, the longer-wavelength impact of lower
211 mantle viscosity is a particular problem. To test the impact of uncertainties in lower-mantle
212 viscosity on the induced intraplate strain fields we show for North America, we also run tests,
213 assessing how much these strain fields vary if we change the lower-mantle viscosity, increasing
214 or decreasing it by factors of 5 and 10 (see Section 4.3).

215 Model time increments are set to 1000 yrs, with the full strain and stress tensors computed
216 at each time interval. Strain- and stress-rate tensors are calculated by differencing the solutions
217 for displacement at adjacent time-steps prior to the calculation of strain and stress tensors.
218 The results shown in Figures 1, 2, and 4 are for the strains at the free surface, and hence are
219 comparable to those measurable at the surface by geodesy or paleoseismology.

220 3 Time/space-variable strain-rates at continental scale

221 Our model results (Figures 1 and 2) show that whilst present-day glaciation-induced strain
222 rates in Europe are low outside of Fennoscandia ($< 5 \times 10^{-9} \text{ yr}^{-1}$), they were significantly
223 greater over much of the Holocene and late Pleistocene than they are at present. In addition,
224 model results show that the strain-rate field was spatially complex (Figure 1) from 40 to
225 about 10 ka, a result of the interplay between the slightly asynchronous evolution of the
226 Fennoscandia/Russian Arctic, British Isles, and Alpine ice sheets (Figure 1a) and the influence
227 of oceanic volume changes. Similarly, horizontal strain rates in North America associated
228 with the growth and decay of Laurentian ice sheet reach $\sim 10^{-7} \text{ yr}^{-1}$ near the ice margins
229 themselves, and exceed $\sim 10^{-8} \text{ yr}^{-1}$ in the continental interior, extending to the Central United
230 States – far in excess of anything observable at the present day at such latitudes [Calais et al.,
231 2006, Kreemer et al., 2014, 2018].

232 Changes in surface load result in an immediate elastic response, which dominates the defor-
233 mation field at short-wavelengths, followed by a slower long-wavelength viscous response, the
234 amplitude of which decays over time as the system re-equilibrates. Ongoing long-wavelength
235 deformation at present in Fennoscandia and northern North America, some 10 ka after the end
236 of major glaciation, is driven by this viscous response (Figure 1f, 3c). The shorter-wavelength
237 ice load over the Alps, for example, is instead predominantly supported elastically, and so
238 produces a rapid, more localised solid-Earth response (Figure 1e), with a smaller, delayed,
239 viscous component.

240 Whilst the large-scale pattern of deformation shown on Figure 1 may appear, to first-order,
241 similar through time, Figure 2 shows that the magnitude and orientation of the principal
242 axes of the horizontal strain-rate tensor goes through a number of rotations and reversals
243 throughout the glacial cycle around the periphery of the major ice sheets. These reversals
244 are most simply observed by considering central Turkey (Figure 2k), a location far enough

245 away from the major ice sheets that the model strain-rates are dominated by the effect of
246 changing sea level in the Black Sea and the eastern Mediterranean rather than by variations
247 of the continental ice mass. One of the principal axes of the horizontal strain-rate tensor
248 is hence always oriented approximately east-west, with a low magnitude. The other axis is
249 consistently oriented approximately north-south, but reverses from compression to extension
250 at around 19 ka, when the global continental ice mass transitions from increase to decrease,
251 with a concomitant shift from sea-level fall to sea-level rise. The notable kink in the N/S-
252 orientated axis at ~ 7 ka is due to the connection of the Black sea to the global ocean system,
253 as previously discussed.

254 Peak strain-rates at any time-step correspond to the location of the largest changes in the
255 surface load as they result from the immediate elastic and initial rapid viscous Earth response.
256 Hence, the largest signal in Figures 1c,d,e is observed within Fennoscandia, at the location of
257 contemporaneous ice load change, and on Figures 3b,c in the areas of Arctic Canada associated
258 with the greatest thickness of the Laurentian icesheet. However, significant strain-rates reach
259 far beyond the ice margins, with a long wavelength viscous response driving crustal deformation
260 across central Europe and western Russia, and extending as far as the Balkans and the north
261 Caspian basin. This large-scale viscous response persists long after the eventual decay of the
262 ice load (Figure 2).

263 Outside the ice margin, the most rapid strain-rate changes are produced instead by the
264 growth and then decay of the Fennoscandian icesheet forebulge, where deformation is domi-
265 nated by the elastic support of the ice margin lithosphere. This is best shown on Figure 1b
266 by the annular structure around the Norwegian coast, through the Baltic states and down to
267 northern Poland, and on Figure 1d by the sharp spike in strain rates through Eastern Europe
268 and Karelia. For North America, this is most apparent on Figure 3c, where the band of high-
269 rate deformation broadly aligns with the Canada/United States border reflects the ongoing

270 collapse of the Laurentian forebulge – a feature detectable with modern GNSS geodesy [e.g.,
271 Calais et al., 2006, Kreemer et al., 2018].

272 The growth and decay of this forebulge and the migration of the strain rate peak with
273 ice growth and removal are particularly relevant to the time-variable strain-rates of both
274 continental Europe and intraplate North America. In Russian Karelia (Figure 2j), a brief
275 period of rapid NW-SE extension between 24 and 19 ka, coincident with the development of
276 the closest part of the Fennoscandian ice sheet at the LGM, is followed by a long interval of
277 low-rate compression, reflecting the gradual decline of ice along the northeastern margin of
278 the ice sheet. A similar time-evolution is seen for the North Sea (Figure 2b). In both of these
279 locations within the Fennoscandian forebulge, model strain-rates are in excess of $5 \times 10^{-8} \text{ yr}^{-1}$,
280 a value that would be easily measured using today’s space geodetic techniques.

281 Across the rest of continental Europe, model strain-rates show significant variations in
282 magnitude and orientation through time that may not be intuitive. In the northern Czech
283 Republic, for example, in addition to variability in the strain-rate magnitude, model results
284 also shows 45° rotation in the orientation of the tensor in ≤ 6 kyrs (Figure 2i). Similarly,
285 Germany, within the forebulge of the Fennoscandian ice sheet and close enough to the Alps
286 to be affected by the effects of Alpine glaciation, presents a complex evolution through time –
287 discussed in more detail in sections 4.1 & 4.2.

288 The effect of ocean margin loading is particularly visible along the coast of North Africa
289 (Figures 1c and 1e). This feature is dominated by the short-wavelength flexure of the margin,
290 resulting in margin-perpendicular extension onshore and compression offshore during times
291 of increasing oceanic volume (continental ice loss – e.g., Figure 1e), and the converse during
292 times of ocean volume decrease (continental ice accrual – e.g., Figure 1c). The flexural effects
293 of ocean margin loading, particularly with respect to strike-slip fault systems, has been previ-
294 ously investigated in detail elsewhere [e.g. Luttrell and Sandwell, 2010, Brothers et al., 2013].

295 Whilst our modelling approach has a more limited spatial resolution and a more simplistic
296 implementation of coastal loading in comparison with that of Luttrell and Sandwell [2010],
297 ours has the advantage that we include long-wavelength effects due to the large-scale ice loads
298 – necessary for regions within ~ 2000 km of the ice margin. In summary, Figures 1, 2, and
299 3 show that strain-rates induced by variations of continental ice masses are heterogeneous in
300 both space and time in regions outside the ice margin. In addition, model results show that
301 this process can result in strain-rates in these regions that are significantly larger than typical
302 tectonic values in stable continental regions ($< 1 \times 10^{-9}$ yr $^{-1}$, Nocquet [2012], Calais et al.
303 [2016]), reaching up to 20×10^{-9} yr $^{-1}$ at the 1000-yr resolution of our model.

304 4 Regional examples

305 Although the above description of model results focuses on strain-rates, the activation of
306 faults should more properly be discussed in terms of the stress, or the changes in stress, acting
307 on them. However, correctly doing so requires *a priori* knowledge of the geometry and slip
308 direction of faults in a given region, information that is rarely available in low-strain rate
309 environments. Additionally, a robust test of the extent to which ice sheet load variations may
310 modulate seismicity would require confronting modelling results with a complete paleoseismic
311 catalogue spanning a period longer than the glacial cycle. Again, such an exhaustive paleo-
312 seismic catalogue is not yet available for either Europe or North America as a whole. In the
313 following, we therefore focus on three of the best-studied areas of intraplate seismicity within
314 continental Europe and North America in terms of paleoseismicity, the European Cenozoic
315 Rift System (ECRS), the Lower Saxony Basin (LSB; Figure 4a), and the New Madrid Seis-
316 mic Zone (NMSZ; Figure 6a). In all cases, significant effort has been put into establishing a
317 paleoseismic record over the Holocene as well as the geometry and slip direction of the major
318 potentially seismogenic faults (e.g., Kockel 2003, Vanneste et al. 2013, Tuttle et al. 2005). We

319 note that there are other regions within central and Northern Europe suggested to have been
320 active over the Holocene (e.g., the Sorgenfrei-Tornquist zone, Brandes et al. [2015, 2018]), but
321 we focus on the ECRS, LSB, and NMSZ, where the fault dip and kinematics are both well
322 known, and consistent across the fault system.

323 4.1 The European Cenozoic Rift System

324 The ECRS system stretches from the northern edge of the Alpine orogeny to the North Sea
325 (Figure 4a). It is split into two sections, the NNE-SSW trending Upper Rhine Graben (URG)
326 and the NW-SE trending Lower Rhine Graben (LRG, also known as the Roer or Rür Valley
327 Graben). The ECRS is one of the most seismically active areas of intraplate Europe and
328 has been the locus of damaging earthquakes, including the M_L 6.1, 1756, Düren earthquake,
329 the M_L 5.8, 1951, Euskirchen earthquake, and more recently the M_L 5.9, 1992, Roermond
330 earthquake with a damage cost estimated at 125 million euros. Seismic hazard within the
331 ECRS is therefore of concern to a number of European nations, given the proximity of several
332 major urban centres, including Strasbourg, Düsseldorf, Köln, and Eindhoven.

333 Geodetic measurements have so far not been able to detect significant tectonic strain across
334 the ECRS [e.g. Nocquet, 2012, Fuhrmann et al., 2015], consistent with the low paleoseismic
335 estimates of average Quaternary fault slip rates ($\leq 0.1 \text{ mm yr}^{-1}$, Vanneste et al. [2013]).
336 Geologically-derived estimates for large earthquake recurrence intervals range from 6 kas to
337 ≥ 80 kas [Vanneste et al., 2001, 2013, Grützner et al., 2016], and hence are comparable to, or
338 longer than, the typical duration of a given orientation of the strain-rates shown in Figures 1
339 and 2.

340 The LRG lies within the forebulge area of the Fennoscandian ice sheet (Figure 2a), where
341 model results show a transient episode of co-glacial extension and deglaciation compression as
342 the ice advances and retreats. The URG is also affected by the time-varying Fennoscandian ice

343 load, but is close enough to the shorter-wavelength Alpine ice load that this has a additional
344 effect. In addition, strain rates in the URG are likely affected by the ongoing erosion taking
345 place across the Alpine orogenic belt, which produces a measurable geodetic strain signal
346 [Sternai et al., 2019], but is not incorporated in our model.

347 Figure 4 shows a close-up of the evolution of strain-rate in north-central Europe as a result
348 of GIA over the past 25 ka. In order to determine whether GIA promotes fault activation of
349 the ECRS bounding faults, we assume, to first order, that failure is promoted when one of
350 principal strain-rate axes is both perpendicular to the fault orientation (points shaded black
351 on the lower panels of Figure 4) and is significantly negative, indicating an increase of the
352 extensional strain.

353 We observe, for both the LRG and URG, a rather complex evolution of the principal axes of
354 the strain rate tensor. At no point do our models indicate that these structures are subjected
355 to simple rift-perpendicular extension. The three-dimensional nature of the strain-rate field
356 rarely produces a strain-rate tensor consistent with uni-directional extension or compression.
357 Even at times where one of the principal axes of the horizontal strain-rate tensor is negative
358 and rift perpendicular, the other axis is typically positive to a similar magnitude and rift-
359 parallel, as demonstrated for the LRG at 19-18 ka (Figure 4c) and the URG over the last 1 ka
360 (Figure 4f).

361 In Figure 5, we calculate rates of change in normal, shear, and Coulomb Failure stress on
362 the LRG, URG, and LSB. All rifts are assumed to comprise pure-dip-slip normal faulting, at
363 a dip of 60° . Coulomb Failure stresses are calculated using an effective coefficient of friction
364 of 0.4. In terms of GIA-induced stress on rift-bounding faults, Figure 5 indicates significantly
365 larger temporal variations in the LRG than in the URG, predominantly due to its closer
366 proximity to the Fennoscandian icesheet. Both grabens show time intervals where failure is
367 enhanced or inhibited by the effects of GIA. In the URG, positive Coulomb stress changes

368 never exceed 0.1 kPA/yr, indicating that the process modelled here likely had minimal impact
369 on fault activation. In the LRG, increased hangingwall sedimentation rates from 15-10 ka have
370 been suggested to be a result of an increase in fault activity (slip rate) during this time period
371 due to the time-variable influence of post-glacial processes [Houtgast et al., 2005]. However,
372 model Coulomb stress changes during this time interval show a (slight) decrease that does not
373 support an increase in normal-faulting activity. Time intervals of increased model Coulomb
374 stress, *e.g.*, from 20-14 ka in the case of the LRG, are not correlated with documented enhanced
375 fault activity, although the total number of earthquakes reported in the LRG over the late
376 Quaternary is relatively small.

377 4.2 Lower Saxony Basin

378 The Lower Saxony Basin in northern Germany (LSB; Figure 4), bounded by WNW-ESE
379 trending faults, initially formed during the Permian as an extensional rift system. Many of
380 these faults were then reactivated as compressional thrust faults during basin inversion in the
381 late Cretaceous-Paleocene [Kockel, 2003], most prominently the Osning thrust at the southern
382 margin of the basin.

383 Trenching across the Osning thrust suggests that a more rapid interval of small-scale ex-
384 tension and inversion occurred over the last glacial cycle Brandes et al. [2012], Brandes and
385 Winsemann [2013], Brandes et al. [2018], with a small amount of extensional slip on the fault
386 during ice advance as the forebulge developed in northern Germany, followed by reversal and
387 thrust motion on the same fault during and following deglaciation as the forebulge collapsed.
388 Figure 4 shows that LSB faults were indeed favourably aligned to the glacially-induced strain-
389 rate field to undergo extension during ice accrual prior to ~ 20 ka, and then reversed to
390 compression from about 16 – 8 ka. Model Coulomb stress changes on Figure 5 are positive,
391 hence consistent with fault activation, during the 16 – 8 ka time interval. However, this does

392 not hold prior to ~ 20 ka.

393 **4.3 The New Madrid Seismic Zone**

394 The New Madrid Seismic Zone (NMSZ; location on Figure 3a) is a region of active intraplate
395 seismicity within the continental interior of North America. Whilst present-day seismicity is
396 typically $<M4$, the area experienced a sequence of large-magnitude ($M>7$) earthquakes in the
397 winter of 1811-1812 [Johnston, 1996, Hough et al., 2000], with geological evidence for other
398 major earthquakes during the Holocene [Tuttle et al., 2005]. Present-day strain rates in the
399 NMSZ are undetectable $- < 1-3 \times 10^{-9} \text{ yr}^{-1}$ [Craig and Calais, 2014, Boyd et al., 2015], leaving
400 the causes of this concentration of intraplate seismicity uncertain. Here, we do not attempt
401 to answer this question, but instead use New Madrid as an example region to investigate the
402 impact of far-field ice-loading on intraplate strain. In Figure 6, we show time-series for strain-
403 and stress-rates at New Madrid driven, and three snapshots of the strain field.

404 Unlike Grollmund and Zoback [2001], we do not include a specific rheologically-weak zone
405 beneath the NMSZ. In Grollmund and Zoback [2001], this serves to focus GIA-induced strain
406 into the region of the NMSZ, producing strain rates capable of producing repetitive seismicity.
407 We instead continue with the radially-symmetric rheological model as described in Section 2,
408 focusing on the longer-wavelength impacts of GIA across the continental interior.

409 The NMSZ consists of a NE-striking, right-lateral strike-slip fault, and a SW-dipping, SE-
410 striking reverse fault, both of which likely ruptured in the 1811-1812 earthquake sequence.
411 Interestingly, our modelling suggests that the strain and stress fields induced by changes in
412 ice-loading in this region, although far too small to have loaded the faults sufficiently in and of
413 themselves, would have been consistent with promoting failure of the strike-slip system between
414 18 – 6 ka, and then promoting failure of the reverse fault system from 5 – 0 ka. Whilst other
415 processes (tectonic or otherwise) must have been involved in loading the faults of the NMSZ

416 to the stage of failure, and are required to explain why earthquakes are concentrated around
417 the NMSZ, and not elsewhere in the continental interior, the removal of the Laurentian ice
418 sheet, under the assumptions made here, would have moved the NMSZ closer to failure.

419 As discussed in Section 2, the deeper viscosity of the mantle plays a dominant role in
420 controlling the longest-wavelengths of induced deformation. However, these viscosities remain
421 poorly constrained, leading to significant uncertainty in the magnitude and decay timescale
422 of the far-field GIA signal – particularly the horizontal components of the strain tensor. To
423 rigorously test the impact that uncertainties in the lower mantle viscosity have on the surface
424 deformation field, varying the viscosity structure should be coupled with a re-determination of
425 the ice history, as the two are derived in combination. Such an endeavour is beyond the scope
426 of our study. Instead, as a test for the impact that uncertainties in lower mantle viscosity may
427 have, we modify the lower mantle viscosity in the structure determined in Zhao et al. [2012], as
428 detailed in Figure S1. As this figure demonstrates, variations in lower mantle viscosity have a
429 major impact on the magnitude of the principal axes of the horizontal strain-rate tensor, with
430 much faster decay in far-field strain-rates for a reduced viscosity. However, the times at which
431 changes are seen in the orientation of far-field strain-rates is more closely related to changes
432 in the growth/decay rate of the ice load, and is relatively insensitive to viscosity.

433 **5 Continental Margin Loading**

434 The effect of changing ocean volumes as a result of variations in continental ice masses on
435 near-marginal faulting has been studied previously, with a particular emphasis on near-coastal
436 transform fault systems [Luttrell and Sandwell, 2010], and marginal fault-related margin slope
437 failure [Brothers et al., 2013]. However, changing ocean volumes, and the strain-fields induced
438 by the resulting flexure of the margin, may affect a wide range of active near-margin fault
439 systems. As shown on Figure 1, strain-rate variations induced by this process can be observed

440 in the model results for the tectonically-active regions of the Atlas margin in North Africa,
441 and the N-S orientated extensional system of western Anatolia.

442 For instance, Figure 2.k illustrates the strain-rate evolution at the eastern end of the ex-
443 tensional systems of Anatolia, in central Turkey. There, the ocean-induced strain field is
444 dominated by the flexure of Anatolia as the volumes of the Black Sea and Eastern Mediter-
445 ranean vary. Model calculations show little variation in E-W strain, but N-S strain-rates that
446 vary between $\pm 5 \times 10^{-9} \text{ yr}^{-1}$. As the geodetically observed present-day strain-rates in that
447 same area are estimated to be around $25 \times 10^{-9} \text{ yr}^{-1}$ [Nocquet, 2012, Piña-Valdés et al., 2022],
448 ocean loading-induced strain may lead to fluctuations of about 20% of the overall extension
449 rates. As a result, one may expect increased rates of seismicity during times when oceanic
450 loading leads to N-S extension, in agreement with the regional tectonics (e.g., 18-7 ka), and
451 decreased earthquake occurrence when the opposite is the case (e.g., 29-20 ka).

452 Similar magnitudes of ocean-loading derived strain-rate are predicted for other active areas,
453 such as Central Greece and peninsular Italy. However, their effect on seismicity rates is likely to
454 be much smaller, due to the significantly greater tectonic strain-rates, in some cases exceeding
455 $100 \times 10^{-9} \text{ yr}^{-1}$ [Nocquet, 2012, Piña-Valdés et al., 2022], and due to less favourable alignments
456 between the secondary and tectonic strain fields than seen in western Anatolia.

457 An alternative example arises from considering the margins of North Africa through Mo-
458 rocco, Algeria, and Tunisia. In these regions – too distal from the major ice sheets for much of
459 a direct deformation signal from changes in glacial loading – the major source of deformation
460 the elastic deformation associated with the changing water levels in the Mediterranean. As
461 such, a simplistic load-induced stress field emerges (visible on Figure 1c,e, in particular), in
462 which, as water level rises, the onshore areas will be subject to an N-S extensional shallow
463 stress change, with deeper N-S compression, which reverse during times of sea level fall. As
464 these regions of North Africa are tectonically active, these induced stress fields, although likely

465 small in comparison to the tectonic stresses, may have a minor modulating effect of the stress
466 accumulation of faults in the region.

467 The values and wavelengths of the deformation associated with continental margin load-
468 ing found here are however dependent on the shallow rheological structure, which is not ac-
469 counted for in the global model used here. As the model parameters used here depend on
470 fitting large-scale observations of glacial isostatic adjustment over continental ice masses that
471 largely coincide with cratonic areas [e.g., Zhao et al., 2012], its average rheology is likely
472 to be stronger, at lithospheric depths, than the non-cratonic continental margins described
473 above. To fully understand the influence of both distal icesheet variations and ocean-loading
474 requires more complex modelling, incorporating regional (and regionally-variable) rheological
475 structures, and, particularly for the ocean-loading problem, the full solution of the sea level
476 equation with time-variable coastlines and topography [Gomez et al., 2018, Whitehouse et al.,
477 2019].

478 **6 Implications for the ‘seismic cycle’**

479 Seismic hazard assessment in continental interiors is often predicated on the assumption that
480 faults behave in a quasi-steady-state manner in which they (1) accumulate stress over time
481 at a steady rate dictated by long-term tectonics, then (2) release the accumulated stress in
482 an earthquake when the shear stress on the fault exceeds its failure limit. In such a model,
483 and in the absence of significant forcing other than long-term tectonics, seismic hazard can
484 therefore be addressed by estimating fault slip rate from space geodesy or paleoseismology and
485 extrapolating it to an earthquake recurrence time and/or an estimated earthquake population
486 [e.g., Rollins and Avouac, 2019, Gerstenberger et al., 2020].

487 We have shown that strain – and hence for an elastic material, stressing – rates likely
488 varied significantly in time and space in continental interiors as a result of glacial isostatic

489 adjustment accompanying variations in icesheets volumes. For instance, in the three cases
490 shown in Figure 5, significant GIA-related strain-rate variations between 40 and 10 ka are
491 followed by negligible variations from ~ 10 ka onward. Hence, seismicity rates in the late
492 Pleistocene and the Holocene may not necessarily be similar to each other for the same fault
493 system. More generally, in areas where non-tectonic processes such as GIA cause significant
494 time-variable strain-rates, the extrapolation of observational, historical, or paleoseismic data
495 – the latter two usually being limited in terms of the number of earthquakes considered –
496 to the present-day seismic hazard comes with the risk of mis-representing which faults are
497 truly active tectonic structures, without additional consideration of what other non-tectonic
498 processes may be impacting on regional earthquake occurrence.

499 The magnitude of stress and strain rates induced by GIA are small compared to tectonic
500 strain rates at plate boundaries or even in slowly deforming regions (typically well excess
501 of 10^{-8} yr^{-1} ; Kreemer et al. [2014]). Moreover, the resulting strain and stress regime can
502 alternate between compression, extension, or strike-slip over short time intervals (Figure 2).
503 It is therefore unlikely that GIA stresses by themselves can bring a fault to its point of failure.
504 However, if most crustal faults are in a state of failure equilibrium and if elastic strain is stored
505 in the bulk of crust [e.g., Zoback and Healy, 1992, Townend and Zoback, 2000], including in
506 stable continental interiors [Craig et al., 2016], then small stress perturbations caused by GIA
507 may be sufficient to modulate and/or trigger seismicity. The stress changes involved are indeed
508 similar to time-dependent stresses caused by hydrological loading that have been demonstrated
509 to modulate seismicity in a variety of tectonic contexts, including stable continental interiors
510 [e.g., Bollinger et al., 2007, Johnson et al., 2017, Craig et al., 2017, Hsu et al., 2021].

511 Figure 7 illustrates in a schematic manner how the superposition of a time-variable and a
512 linear background tectonic stressing-rate may affect the timing of earthquake occurrence in a
513 given area. We assume that earthquakes repeat for the same amount of accumulated stress

514 within a given area and that there is always a favourably oriented fault able to rupture when
515 that state is reached. The total stress build-up is the sum of the time-variable stressing-rate
516 and of a linear, background, tectonic stressing-rate. The latter may be extremely small in
517 stable continental regions, where strain rates are typically $< 2 \times 10^{-9} \text{ yr}^{-1}$ [Kreemer et al.,
518 2018, Masson et al., 2019].

519 This simple conceptual model has several corollaries:

520 • Firstly, the presence of time-dependent stress obviously advances or delays the occur-
521 rence of earthquakes compared to a model where only tectonic stress is acting. This
522 introduces a variability in the inter-event time compared to a theoretical, purely steady-
523 state, system, in which earthquake occurrence would be regular and monotonic.

524 • Secondly, the variability of the inter-event time depends on the amplitude of the time-
525 dependent stress changes with respect to the constant background tectonic stressing-rate.
526 At the limit, if the latter is extremely small, such as in stable continental regions, then
527 inter-event time depends solely on non-tectonic, time-dependent stress changes and may
528 be very variable, and potentially non-repetitive. Conversely, if the tectonic stressing rate
529 is large compared to time-dependent stress changes, such as at an active plate boundary,
530 inter-event time will be much less variable as they are mostly dictated by the background
531 tectonic loading. In the simple example shown in Figure 7, the inter-event time varies
532 by $\sim 50\%$.

533 • Thirdly, the superposition of the time-variable signal results in time intervals where the
534 failure of well-oriented faults may be promoted (advanced) or delayed. In cases where
535 the amplitude of the time-variable signal exceeds that of the background stressing rate,
536 this can go so far as to produce time intervals where the fault failure is inhibited.

537 Note that the illustrative model shown here in Figure 7 treats failure as a simple threshold

538 process, and includes no complex fault mechanics. The periods involved are long enough that
539 processes relating to the nucleation of individual earthquakes are unlikely to matter. However,
540 the frictional processes governing the accumulation, maintenance, and release of stress on
541 individual fault planes are likely to lead to further complexity and variability in the temporal
542 distribution of earthquakes on faults where such secondary processes are present that we do
543 not attempt to quantify here. In the particular case of glacially-related load changes, there
544 are also potential issues relating to fluxing of glacially-derived fluids through the upper crust,
545 and the resulting changes in pore-fluid pressures, that we also do not consider in our simple
546 model.

547 **7 Conclusion**

548 We have demonstrated how strain-rates vary in space and time in Europe and North America
549 solely as a result of the growth and decay of the Eurasian and Laurentian ice sheets since 40 ka.
550 We show that such non-tectonic forcing can significantly influence the overall strain-rate field,
551 and hence stresses that apply on faults within roughly one wavelength of the ice margin, in
552 a rather complicated manner that includes both the effects of changes in ice and ocean mass
553 distributions.

554 Overall, the time-dependent pattern of GIA-induced strain-rate variations in Europe is
555 dominated by the variability of the mass of the Fennoscandian icesheet, with smaller contribu-
556 tions from British Isles and Alpine glaciers. Continental margin loading as a result of icesheet
557 melting adds a secondary complexity to the strain-rate variation pattern. Deformation com-
558 prises both the immediate elastic response to changes in load, particularly dominant at short
559 wavelengths, and the viscous response, which dominates at longer wavelengths and over longer
560 timescales. Model results indicate that strain-rates – and hence stresses that apply on faults
561 – can be significant, with large spatial and temporal variations, during the late Pleistocene

562 and peaking around the time of LGM. In some cases, the induced crustal stressing rates likely
563 exceed the local tectonic stressing rates. Variations are much smaller over the Holocene, with
564 the decay of major postglacial deformation across Europe, and are generally negligible after
565 about 6 ka.

566 In regions where the background tectonic stressing rates are similar to, or smaller than, the
567 superimposed non-tectonic rates, such effects can lead to time intervals where fault failure is
568 advanced, delayed, or inhibited, depending on the alignment of the given fault system with the
569 overall stress field. As a result, earthquake occurrence within given fault systems may become
570 irregular, with long intervals of quiescence or bursts of enhanced activity. Whilst we lack
571 sufficient paleoseismological data for a full assessment of the degree to which such variations
572 influenced seismicity over this period, we recommend consideration of such effects in low-strain
573 environments, as they add an additional uncertainty when using either modern-day geodetic
574 strain rate fields, seismological records, or paleoseismic slip-rates based on small numbers of
575 earthquakes, for long term seismic hazard assessment.

576 **Acknowledgements**

577 This work was funded through the French Investment Program SINAPS@ project by the
578 Commissariat à l'Énergie Atomique and the Institute de Radioprotection et Sûreté Nucléaire,
579 and was hosted by the LRC Yves Rocard (Laboratoire de Recherche Conventionné CEA-ENS-
580 CNRS). TJC also thanks the Royal Society (under URF\R1\180088) for financial support
581 during the final stages of this project. EC acknowledges funding from the Institut Universitaire
582 de France. We thank K. Lambeck for making the ANU-ICE model available, and C. Gruetzner
583 for his assistance with Rhine Graben data. Figures were created using the Generic Mapping
584 Tools software package.

References

- 585
586 Z. Alterman, H. Jarosch, and C.L. Pekeris. Oscillations of the Earth. *Proceedings of the*
587 *Royal Society A*, 252, 1959. doi: 10.1098/rspa.1959.0138.
- 588 C. B. Amos, P. Audet, W. C. Hammond, R. Bürgmann, I. A. Johanson, and G. Blewitt. Uplift
589 and seismicity driven by groundwater depletion in central California. *Nature*, 509:483–486,
590 2014. doi: 10.1038/nature13275.
- 591 P. Bettinelli, J.-P. Avouac, M. Flouzat, L. Bollinger, G. Ramillien, S. Rajaure, and S. Sap-
592 kota. Seasonal variations of seismicity and geodetic strain in the Himalaya induced
593 by surface hydrology. *Earth and Planetary Science Letters*, 266:332–344, 2007. doi:
594 10.1016/j.epsl.2007.11.021.
- 595 L. Bollinger, F. Perrier, J.-P. Avouac, S. Sapkota, U. Gautam, and D.R. Tiwari. Seasonal
596 modulation of seismicity in the Himalaya of Nepal. *Geophysical research Letters*, 34, 2007.
597 doi: 10.1029/2006GL029192.
- 598 O. S. Boyd, R. Smalley Jr., and Y. Zeng. Crustal deformation in the New Madrid seismic
599 zone and the role of postseismic processes. *Journal of Geophysical Research*, 120:5782–5803,
600 2015. doi: 10.1002/2015JB012049.
- 601 C. Brandes and J. Winsemann. Soft-sediment deformation structures in NW Germany caused
602 by Late Pleistocene seismicity. *International Journal of Earth Sciences*, 102:2255–2274,
603 2013. doi: 10.1007/s00531-013-0914-4.
- 604 C. Brandes, J. Winsemann, J. Roskosch, J. Meinsen, D. C. Tanner, M. Frechen, H. Steffen,
605 and P. Wu. Activity along the Osning Thrust in Central Europe during the Lateglacial:
606 ice-sheet and lithosphere interactions. *Quaternary Science Reviews*, 38:49–62, 2012. doi:
607 10.1016/j.quascirev.2012.01.021.

608 C. Brandes, H. Steffen, R. Steffen, and P. Wu. Intraplate seismicity in northern Central Europe
609 is induced by the last glaciation. *Geology*, 43:611–614, 2015. doi: 10.1130/G36710.1.

610 C. Brandes, H. Steffen, P.B.E. Sandersen, P. Wu, and J. Winsemann. Glacially induced faulting
611 along the NW segment of the Sorgenfrei-Tornquist Zone, northern Denmark: Implication
612 for neotectonics and Lateglacial fault-bound basin formation. *Quaternary Science Reviews*,
613 189:149–168, 2018. doi: 10.1016/j.quarscirev.2018.03.036.

614 D. S. Brothers, K. M. Luttrell, and J. D. Chaytor. Sea-level-induced seismicity and submarine
615 landslide occurrence. *Geology*, 41(9):979–982, 2013.

616 E. Calais and S. Stein. Time-Variable Deformation in the New Madrid Seismic Zone. *Science*,
617 323:1442, 2009. doi: 10.1226/science.1168122.

618 E. Calais, J. Y. Han, C. DeMets, and J. M. Noquet. Deformation of the North American plate
619 interior from a decade of continuous GPS measurements. *Journal of Geophysical Research*,
620 111, 2006. doi: 10.1029/2005JB004253.

621 E. Calais, A. M. Freed, R. Van Arsdale, and S. Stein. Triggering of New Madrid Seismicity
622 by late-Pleistocene erosion. *Nature*, 466, 2010. doi: 10.1038/nature09258.

623 E. Calais, T. Camelbeeck, S. Stein, M. Liu, and T.J. Craig. A new paradigm for large earth-
624 quakes in stable continental plate interiors. *Geophysical Research Letters*, 43:10621–10637,
625 2016. doi: 10.1002/2016GL070815.

626 T. Camelbeeck, K. Vanneste, P. Alexandre, K. Verbeeck, T. Petermans, P. Rosset, M. Ever-
627 aerts, R. Warnant, and M. Van Camp. Relevance of active faulting and seismicity studies to
628 assessment of long-term earthquake activity and maximum magnitude in intraplate north-
629 west Europe, between the Lower Rhine Embayment and the North Sea. *Geological Society
630 of America Special Paper*, 425:193–224, 2007. doi: 10.1130/2007.2425(14).

-
- 631 L. Caron, L. Métivier, M. Greff-Lefftz, L. Fleitout, and H. Rouby. Inverting Glacial Isostatic
632 Adjustment signal using Bayesian framework and two linearly relaxing rheologies. *Geophys-*
633 *ical Journal International*, 209:1126–1147, 2017. doi: 10.1093/gji/ggx083.
- 634 L. Cathles. *Viscosity of the Earths Mantle*. Princeton University Press, 1975.
- 635 T. J. Craig and E. Calais. Strain accumulation in the New Madrid and Wabash Valley Seismic
636 Zones from 14 years of continuous GPS observation. *Journal of Geophysical Research*, 119:
637 1–20, 2014. doi: 10.1002/2014JB011498.
- 638 T. J. Craig, E. Calais, L. Fleitout, L. Bollinger, and O. Scotti. Evidence for the release
639 of long-term tectonic strain stored in continental interiors through intraplate earthquakes.
640 *Geophysical Research Letters*, 43:6826–6836, 2016. doi: 10.1002/2016GL069359.
- 641 T. J. Craig, K. Chanard, and E. Calais. Hydrologically-driven crustal stresses and seismicity
642 in the New Madrid Seismic Zone. *Nature Communications*, 8, 2017. doi: 10.1038/s41467-
643 017-01696-w.
- 644 A.M. Dziewonski and D.L. Anderson. Preliminary reference Earth model. *Physics of the Earth*
645 *and Planetary Interiors*, 25, 1981. doi: 10.1016/0031-9201(81)90046-7.
- 646 T. Fuhrmann, M. Caro Cuenca, A. Knöpfler, F.J. van Leijen, M. Mayer, M. Westerhaus,
647 R.F. Hanssen, and B. Heck. Estimation of small surface displacements in the Upper Rhine
648 Graben area from a combined analysis of PS-InSAR, levelling and GNSS data. *Geophysical*
649 *Journal International*, 203:614–631, 2015. doi: 10.1093/gji/ggv328.
- 650 M.C. Gerstenberger, W. Marzocchi, T. Allen, M. Pagani, J. Adams, L. Danciu, E.H. Field,
651 H. Fujiwara, N. Luco, K.-F. Ma, C. Meletti, and M.D. Petersen. Probabilistic Seismic
652 Hazard Analysis at Regional and National Scales: State of the Art and Future Challenges.
653 *Reviews of Geophysics*, 58, 2020. doi: 10.1029/2019RG000653.

-
- 654 N. Gomez, K. Latychev, and D. Pollard. A Coupled Ice Sheet-Sea Level Model Incorporating
655 3D Earth Structure: Variations in Antarctica during the Last Deglacial Retreat. *Journal of*
656 *Climate*, 31:4041–4054, 2018. doi: 10.1175/JCLI-D-17-0352.1.
- 657 B. Grollmund and M. D. Zoback. Did deglaciation trigger intraplate seismicity in the New
658 Madrid seismic zone. *Geology*, 29:175–178, 2001.
- 659 G. Grünthal and R. Wahlström. The European-Mediterranean Earthquake Catalogue (EMEC)
660 for the last millennium. *Journal of Seismology*, 16:535–570, 2012. doi: 10.1007/s10950-012-
661 9302-y.
- 662 C. Grützner, P. Fischer, and K. Reicherter. Holocene surface ruptures of the Rurrand Fault,
663 Germany – insights from palaeoseismology, remote sensing and shallow geophysics. *Geo-*
664 *physical Journal International*, 204:1662–1677, 2016. doi: 10.1093/gji/ggv558.
- 665 A. Hampel, R. Hetzel, and A.L. Densmore. Postglacial slip-rate increase on the Teton normal
666 fault, northern Basin and Range Province, caused by melting of the Yellowstone ice cap and
667 deglaciation of the Teton Range? *Geology*, 35:1107–1110, 2007. doi: 10.1130/G24093A.1.
- 668 K. Heki. Snow load and seasonal variation of earthquake occurrence in Japan. *Earth and*
669 *Planetary Science Letters*, 207:159–164, 2003.
- 670 S. E. Hough and M. Page. Toward a consistent model for strain accrual and release for the
671 New Madrid Seismic Zone, central United States. *Journal of Geophysical Research*, 116,
672 2011. doi: 10.1029/2010JB007783.
- 673 S. E. Hough, J. G. Armbruster, L. Seeber, and J. F. Hough. On the modified Mercalli inten-
674 sities and magnitudes of the 1811–1812 New Madrid earthquakes. *Journal of Geophysical*
675 *Research: Solid Earth (1978–2012)*, 105(B10):23839–23864, 2000.

676 R. F. Houtgast, R. T. Van Balen, and C. Kasse. Late Quaternary evolution of the Feld-
677 biss Fault (Roer Valley Rift System, the Netherlands) based on trenching, and its poten-
678 tial relation to glacial unloading. *Quaternary Science Reviews*, 24:491–510, 2005. doi:
679 10.1016/j.quascirev.2004.01.012.

680 Y.-J. Hsu, H. Kao, R. Burgmann, Y.-T. Lee, H.-H. Huang, Y.-F. Hsu, Y.-M. Wu, and
681 J. Zhuang. Synchronized and asynchronous modulation of seismicity by hydrological loading:
682 A case study in Taiwan. *Science Advances*, 7, 2021. doi: 10.1126/sciadv.abf7282.

683 Christopher W Johnson, Yuning Fu, and Roland Bürgmann. Seasonal water storage, stress
684 modulation, and California seismicity. *Science*, 336:1161–1164, June 2017.

685 A. C. Johnston. Seismic moment assessment of stable continental earthquakes – III. 1811-1812
686 New Madrid, 1886 Charleston, and 1755 Lisbon. *Geophysical Journal International*, 126:
687 314–344, 1996.

688 H. P. Kierulf, H. Steffen, M. J. R. Simpson, M. Lidberg, P. Wu, and H. Wang. A GPS velocity
689 field for Fennoscandia and a consistent comparison to glacial isostatic adjustment models.
690 *Journal of Geophysical Research*, 119, 2014. doi: 10.1002/2013JB010889.

691 F. Kockel. Inversion structures in Central Europe – expressions and reasons, and open discus-
692 sion. *Netherlands Journal of Geosciences*, 235:277–291, 2003.

693 C. Kreemer, G. Blewitt, and E.C. Klein. A geodetic plate motion and Global
694 Strain Rate Model. *Geochemistry, Geophysics, Geosystems*, 14:3849–3889, 2014. doi:
695 10.1002/2014GC005407.

696 C. Kreemer, W.C. Hammond, and G. Blewitt. A Robust Estimation of the 3-D Intraplate
697 Deformation for the North American Plate From GPS. *Journal of Geophysical Research*, 123:
698 4388–4412, 2018. doi: 10.1029/2017JB015257.

-
- 699 R. Lagerbäck and M. Sundh. Early Holocene faulting and paleoseismicity in Northern Sweden.
700 *Sveriges geologiska undersökning – Research paper, Uppsala, Sweden, C 836, 2008.*
- 701 Mian Liu and Seth Stein. Mid-continental earthquakes: Spatiotemporal occurrences, causes,
702 and hazards. *Earth Science Reviews*, 162:364–386, November 2016.
- 703 K. Luttrell and D. Sandwell. Ocean loading effects on stress at near shore plate boundary
704 fault systems. *Journal of Geophysical Research*, 115, 2010. doi: 10.1029/2009JB006541.
- 705 K. Luttrell, D. Sandwell, B. Smith-Konter, B. Bills, and Y. Bock. Modulation of the earthquake
706 cycle at the southern San Andreas fault by lake loading. *Journal of Geophysical Research*,
707 112, 2007. doi: 10.1029/2006JB004752.
- 708 C. Masson, S. Mazzotti, P. Vernant, and E. Doerflinger. Extracting small deformation beyond
709 individual station precision from dense Global Navigation Satellite System (GNSS) networks
710 in France and western Europe. *Solid Earth*, 10:1905–1920, 2019. doi: 10.5194/de-10-1905-
711 2019.
- 712 S. Mazzotti, T.S. James, J. Henton, and J. Adams. GPS crustal strain, postglacial rebound,
713 and seismic hazard in eastern North America: The Saint Lawrence valley example. *Journal*
714 *of Geophysical Research*, 110, 2005. doi: 10.1029/2004JB003590.
- 715 R. Muir-Wood. Extraordinary deglaciation reverse faulting in northern Fennoscandia. In
716 S. Gregersen and P. W. Basham, editors, *Earthquakes at North Atlantic passive margins:*
717 *Neotectonics and post-glacial rebound*, NATO ASI Series, pages 141–174. Springer, 1989.
- 718 J.-M. Nocquet. Present-day kinematics of the Mediterranean: A comprehensive overview of
719 GPS results. *Tectonophysics*, 579:220–242, 2012. doi: 10.1016/j.tecto.2012.03.037.
- 720 J.-M. Nocquet, E. Calais, and B. Parsons. Geodetic constraints on glacial isostatic adjustment
721 in Europe. *Geophysical Research Letters*, 32, 2005.

-
- 722 A.E.K. Ojala, J. Mattila, J. Hämäläinen, and R. Sutinen. Lake sediment evidence of paleo-
723 seismicity: Timing and spatial occurrence of late- and postglacial earthquakes in Finland.
724 *Tectonophysics*, 771, 2019. doi: 10.1016/j.tecto.2019.228227.
- 725 W.R. Peltier. Global Glacial Isostasy and the Surface of the Ice-Age Earth: The ICE-5G
726 (VM2) Model and GRACE. *Annual Review of Earth and Planetary Science*, 32:111–149,
727 2004.
- 728 W.R. Peltier and R. Drummond. Rheological stratification of the lithosphere: A direct
729 inference based upon the geodetically observed pattern of the glacial isostatic adjuste-
730 ment of the North American continent. *Geophysical Research Letters*, 35, 2008. doi:
731 10.1029/2008GL034586.
- 732 J. Piña-Valdés, A. Socquet, C. Beauval, M.-P. Doin, N. D’Agostino, and Z.-K. Shen. 3D
733 GNSS Velocity Field Sheds Light on the Deformation Mechanisms in Europe: Effects of the
734 Vertical Crustal Motion on the Distribution of Seismicity. *Journal of Geophysical Research*,
735 127, 2022. doi: 10.1029/2021JB023451.
- 736 C. Rollins and J.-P. Avouac. A Geodesy- and Seismicity-Based Local Earthquake Likelihood
737 Model for Central Los Angeles. *Geophysical Research Letters*, 46:3153–3162, 2019. doi:
738 10.1029/2018GL080868.
- 739 W. B. F. Ryan, C. O. Major, G. Lericolais, and S. L. Goldstein. Catastrophic flooding of
740 the Black Sea. *Annual Reviews in Earth and Planetary Sciences*, 31:525–554, 2003. doi:
741 31.100901141249.
- 742 J. Sauber and N. A. Ruppert. Rapid Ice Mass Loss: Does It Have an Influence on Earthquake
743 Occurrence in Southern Alaska? In J. T. Freymueller, P. J. Haeussler, R. L. Wesson,
744 and G. Ekström, editors, *Active Tectonics and Seismic Potential of Alaska*, volume 179 of
745 *Geophysical Monograph*. American Geophysical Union, 2008. doi: 10.1029/179GM21.

-
- 746 J. M. Sauber and B. F. Molnia. Glacier ice mass fluctuations and fault instability in tec-
747 tonically active southern alaska. *Global and Planetary Change*, 42:279–293, 2004. doi:
748 10.1016/j.gloplacha.2003.11.012.
- 749 Seth Stein, Robert J Geller, and Mian Liu. Why earthquake hazard maps often fail and what
750 to do about it. *Tectonophysics*, 562-563:1–25, August 2012.
- 751 P. Sternai, C. Sue, L. Husson, E. Serpelloni, T.W. Becker, S.D. Willett, C. Faccenna, A. Di
752 Giulio, G. Spada, L. Jolivet, P. Valla, C. Petit, J.-M. Nocquet, A. Walpersdorf, and
753 S. Castelltort. Present-day uplift of the European Alps: Evaluating mechanisms and
754 models of their relative contributions. *Earth-Science Reviews*, 190:589–604, 2019. doi:
755 10.1016/j.earscirev.2019.01.005.
- 756 J. Townend and M. D. Zoback. How faulting keeps the crust strong. *Geology*, 28(5):399–402,
757 2000.
- 758 M. P. Tuttle, E. S. Schwieg III, J. Campbell, P. N. Thomas, J. D. Sims, and R. H. Lafferty III.
759 Evidence for New Madrid Earthquakes in A.D. 300 and 2350 B.C. *Seismological Research*
760 *Letters*, 76:489–502, 2005.
- 761 R.T. Van Balen, M.A.J. Bakker, C. Kasse, J. Wallinga, and H.A.G. Wolferink. A
762 Late Glacial surface rupturing earthquake at the Peel Boundary fault zone, Roer Val-
763 ley Rift System, the Netherlands. *Quaternary Science Reviews*, 218:254–266, 2019. doi:
764 10.1016/j.quascirev.2019.06.033.
- 765 K. Vanneste, K. Verbeek, T. Camelbeek, E. Paulissen, M. Meghraoui, F. Renardy, D. Jong-
766 mans, and M. Frechen. Surface-rupturing history of the Bree fault scarp, Roer Valley graben:
767 Evidence for six events since the late Pleistocene. *Journal of Seismology*, 5:329–359, 2001.
- 768 K. Vanneste, T. Camelbeek, and K. Verbeek. A Model of Composite Seismic Sources for the

-
- 769 Lower Rhine Graben, Northwest Europe. *Bulletin of the Seismological Society of America*,
770 103:984–1007, 2013. doi: 10.1785/0120120037.
- 771 P. Štěpančíková, J. Hók, D. Nývlt, J. Dohnal, I. Sýkorová, and J. Stemberk. Active tectonics
772 research using trenching technique on the south-eastern section of the Sudetic Marginal
773 Fault (NE Bohemian Massif, central Europe). *Tectonophysics*, 485:269–282, 2012. doi:
774 10.1016/j.tecto.2010.01.004.
- 775 P. Štěpančíková, T. Fischer, J. Stemberk, L. Nováková, f. Hartvich, and P.M. Figueiredo.
776 Active tectonics on the Cheb Basin: youngest documented Holocene surface faulting in
777 Central Europe. *Geomorphology*, 327:472–488, 2019. doi: 10.1016/j.geomorph.2018.11.007.
- 778 P. Štěpančíková, T.K. Rockwell, J. Stemberk, E.J. Rhodes, F. Hartvich, K. Luttrell, M. Myers,
779 P. Tábořík, D.H. Rood, N. Wechsler, D. Nývlt, M. Ortuno, and J. Hók. Acceleration of Late
780 Pleistocene activity of a Central European fault driven by ice loading. *Earth and Planetary
781 Science Letters*, 591, 2022. doi: 10.1016/j.epsl.2022.117596.
- 782 P. Whitehouse, N. Gomez, M. A. King, and D. A. Wiens. Solid Earth change and the evolution
783 of the Antarctica Ice Sheet. *Nature Communications*, 10, 2019. doi: 10.1038/s41467-018-
784 08068-y.
- 785 P. Wu, P. Johnston, and K. Lambeck. Post-glacial rebound and fault instability in
786 Fennoscandia. *Geophysical Journal International*, 139:657–670, 1999. doi: 10.1046/j.1365-
787 246x.1999.00963.x.
- 788 S. Zhao, K. Lambeck, and M. Lidberg. Lithosphere thickness and mantle viscosity inverted
789 from GPS-derived deformation rates in Fennoscandia. *Geophysical Journal International*,
790 190, 2012. doi: 10.1111/j.1365-246X.2012.05454.x.
- 791 M. D. Zoback and J. H. Healy. In situ stress measurements to 3.5 km depth in the Cajon Pass

792 Scientific Research Borehole: Implications for the mechanics of crustal faulting. *Journal of*
793 *Geophysical Research*, 97:5039–5057, 1992.

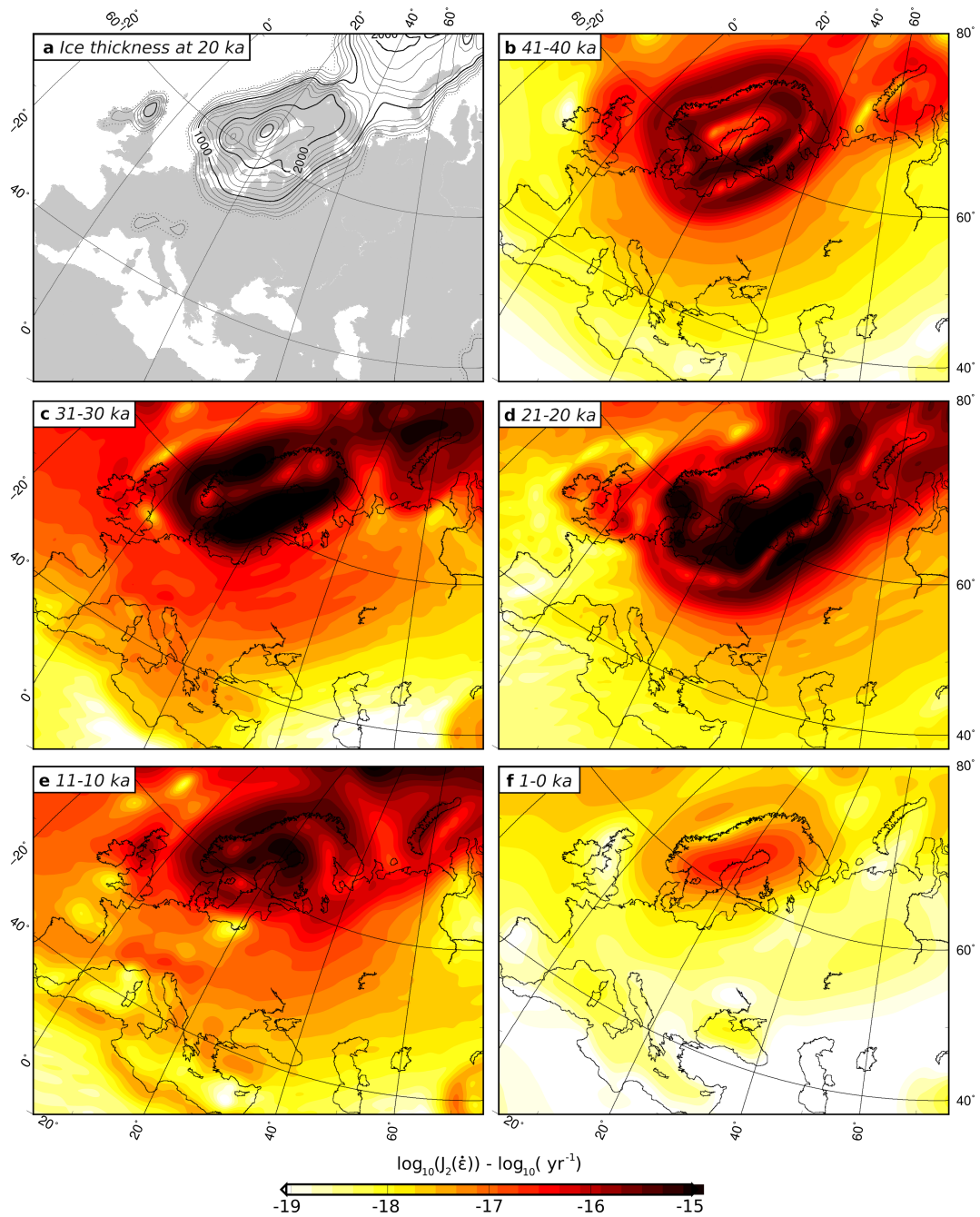


Figure 1: **Strain-rate distribution across Europe.** (a) Ice volume at 20 ka from ANU-ICE. Solid contours are at 200 m intervals. Dashed contour is the 100 m contour, as a proxy for the ice margin. (b)-(f) Second invariant of the deviatoric strain-rate tensor at (b) 41-40 ka, (c) 31-30 ka, (d) 21-20 ka, (e) 11-10 ka, (f) 1-0 ka. The scale used is the same in each case. All results are calculated at the free surface.

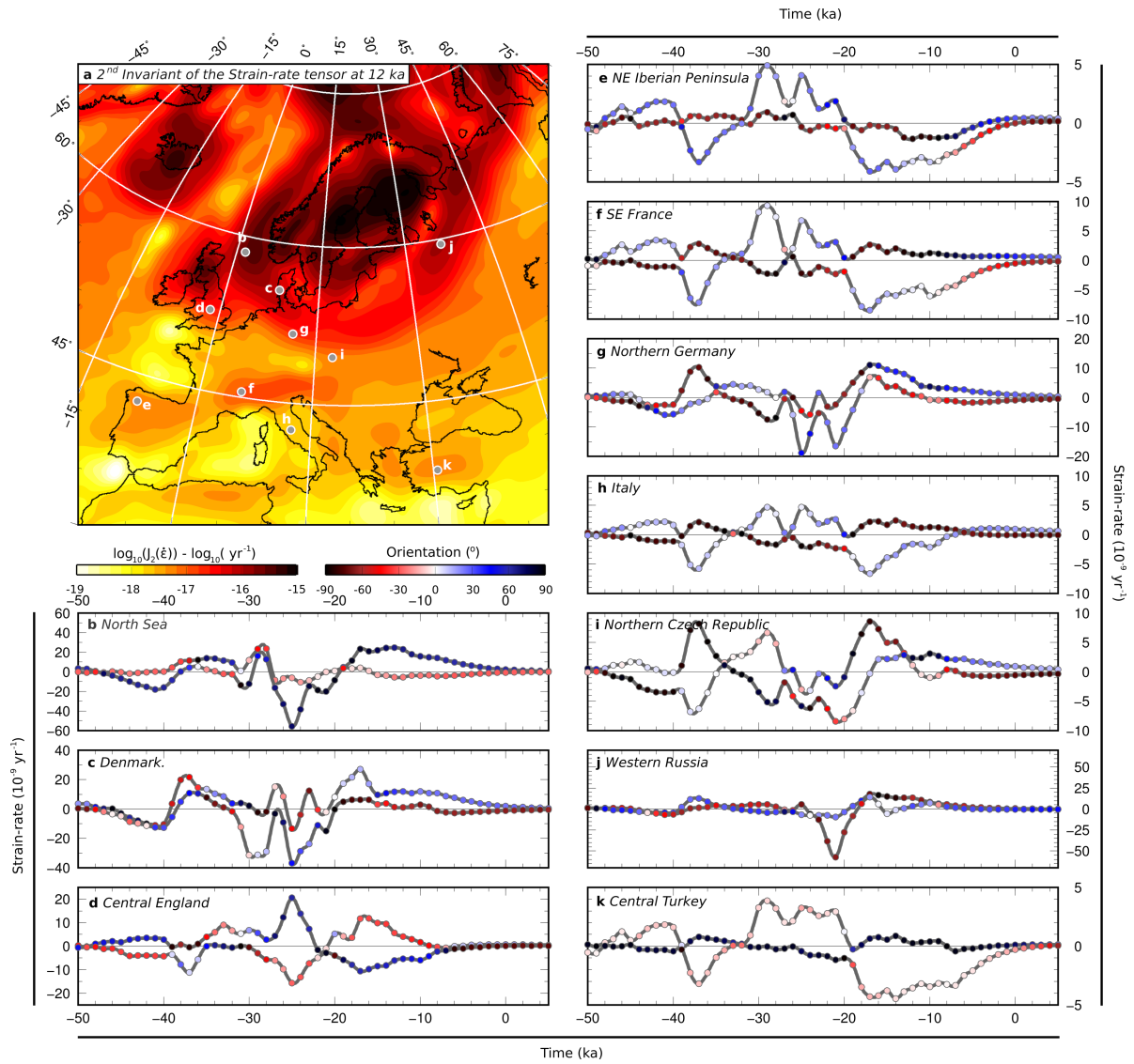


Figure 2: **Strain-rate time series across Europe.** (a) Second invariant of the deviatoric strain-rate tensor at 13-12 ka. (b)-(k) Profiles of the principal axes of the horizontal strain-rate tensor through time at the locations shown on (a). Points are coloured to indicates the orientation (in azimuth clockwise from north) of each axis. Note that the strain-rate scale is different on each profile. All results are calculated at the free surface.

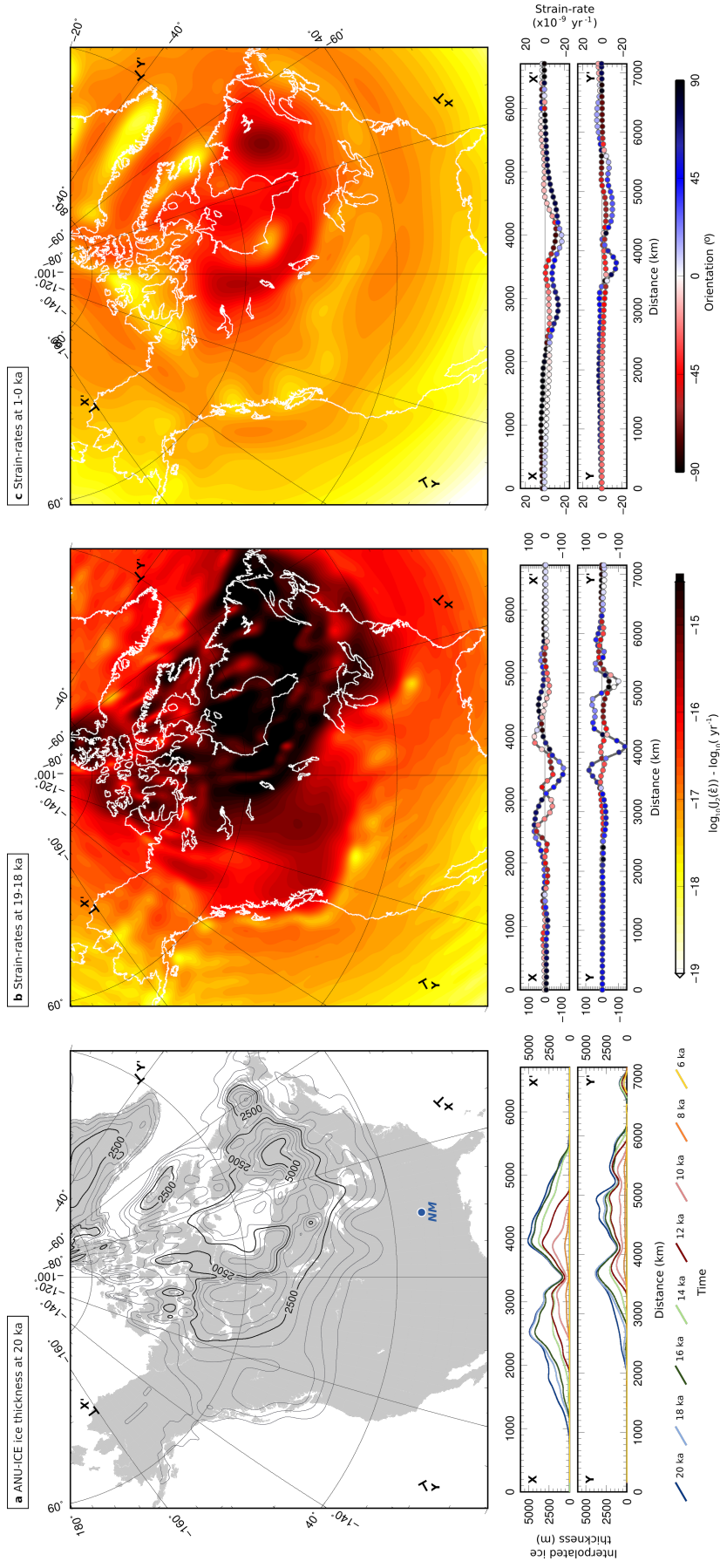


Figure 3: Strain rates in North America. (a) Ice extents at 20 ka from ANU-ICE. Solid contours are at 500 m intervals. Lower panels show profiles as indicated on the map, with ice sheet thicknesses at 20 ka to 6 ka. (b) Second invariant of the strain-rate tensor at 19-18 ka. Lower panels show profiles, indicating the magnitudes and (as symbol colour) orientation of the principal axes of the strain rate tensor. (c) as in (b), but for 1-0 ka. Note that the scale in the lower panels is reduced by 1/5 in comparison to (b).

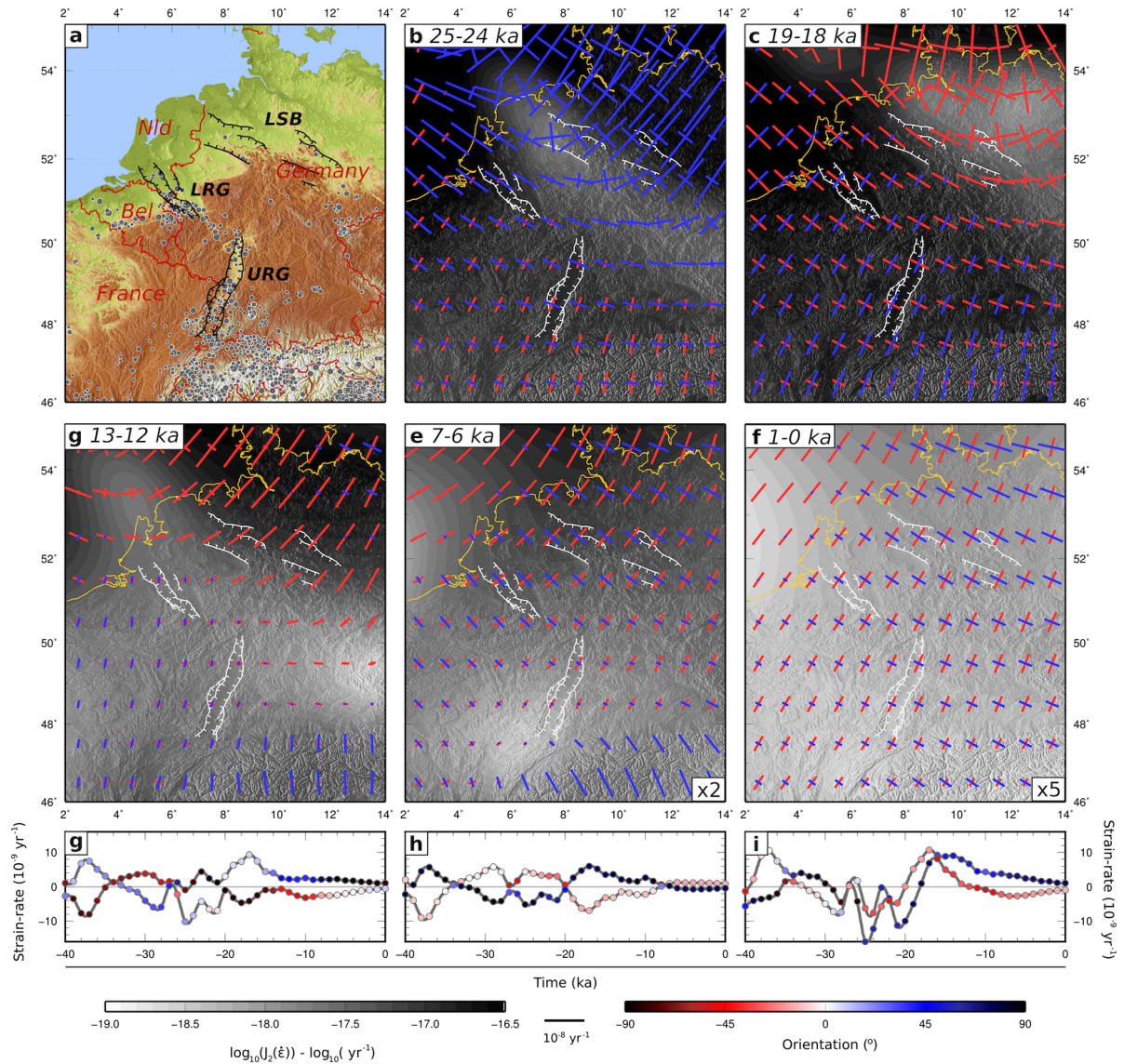


Figure 4: **Strain-rate evolution in the European Cenozoic Rift System.** (a) The Cenozoic European Rift System. Grey dots are earthquakes from the European-Mediterranean Earthquake Catalogue for 1000-2006 [Grünthal and Wahlström, 2012], filtered for $M_W > 3.5$, and scaled by magnitude. Black lines are the fault systems of the Upper and Lower Rhine Graben after Vanneste et al. [2013], and the North German Basin after Brandes et al. [2012]. The sense of motion shown is based on the Cenozoic motion of the fault, and may differ from the sense of motion in recent earthquakes, where reactivation has occurred. Bel: Belgium. Nld: Netherlands. LRG: Lower Rhine Graben. URG: Upper Rhine Graben. LSB: Lower Saxony Basin. (b) - (f) Principal axes of the horizontal strain-rate tensor (coloured bars, blue for extension, red for compression), overlain on the second invariant of the deviatoric strain-rate tensor. The time interval displayed is shown in the top left corner of each panel. The scale for strain-rate crosses is multiplied by a factor of 2 on panel (e) and a factor of 5 on panel (f), to make the results visible. (g),(h),(i) Evolution of the principal axes of the horizontal strain-rate tensor for the Lower Rhine Graben, Upper Rhine Graben and Lower Saxony Basin, respectively. Point colour on (g),(h),(i) indicates the angle between the principal strain axis and each fault system fault system.

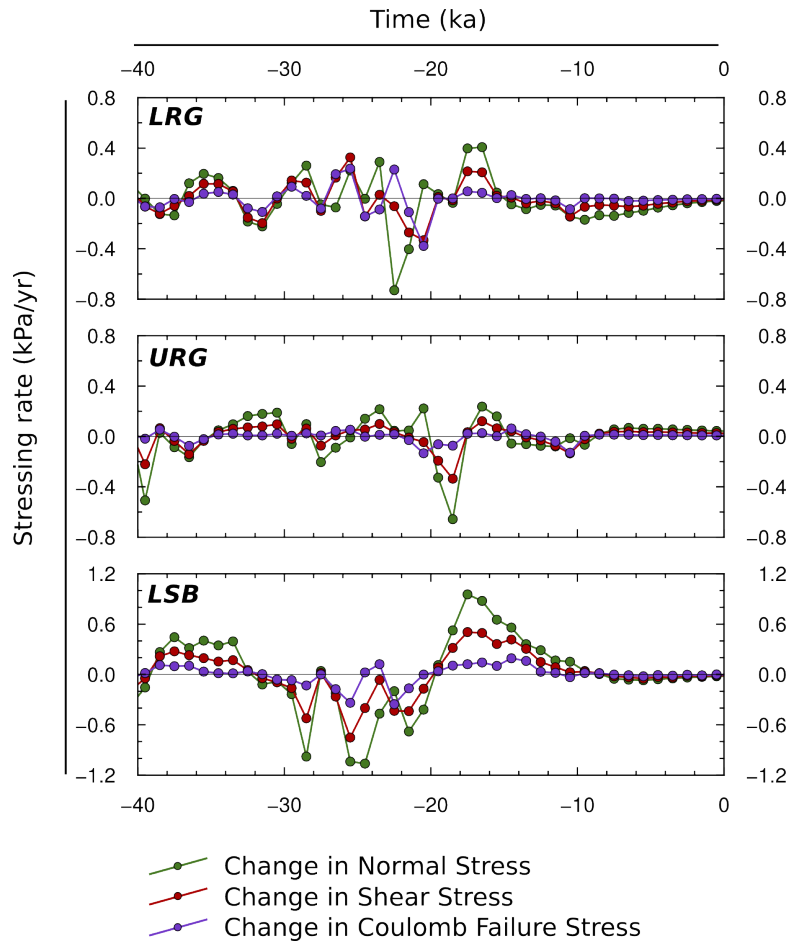


Figure 5: **Stressing-rate evolution in the European Cenozoic Rift System.** Each panel shows the time-variation in glacially-induced stressing rate in terms of normal, shear, and a Coulomb Failure stress, for the Lower Rhine Graben (top panel), Upper Rhine Graben (middle panel), and Lower Saxony Basin (bottom panel). Stress is calculated at 10 km depth assuming planar faults with a geometry based on their surface strike, a dip angle of 60° , and pure dip-slip, normal faulting, motion.

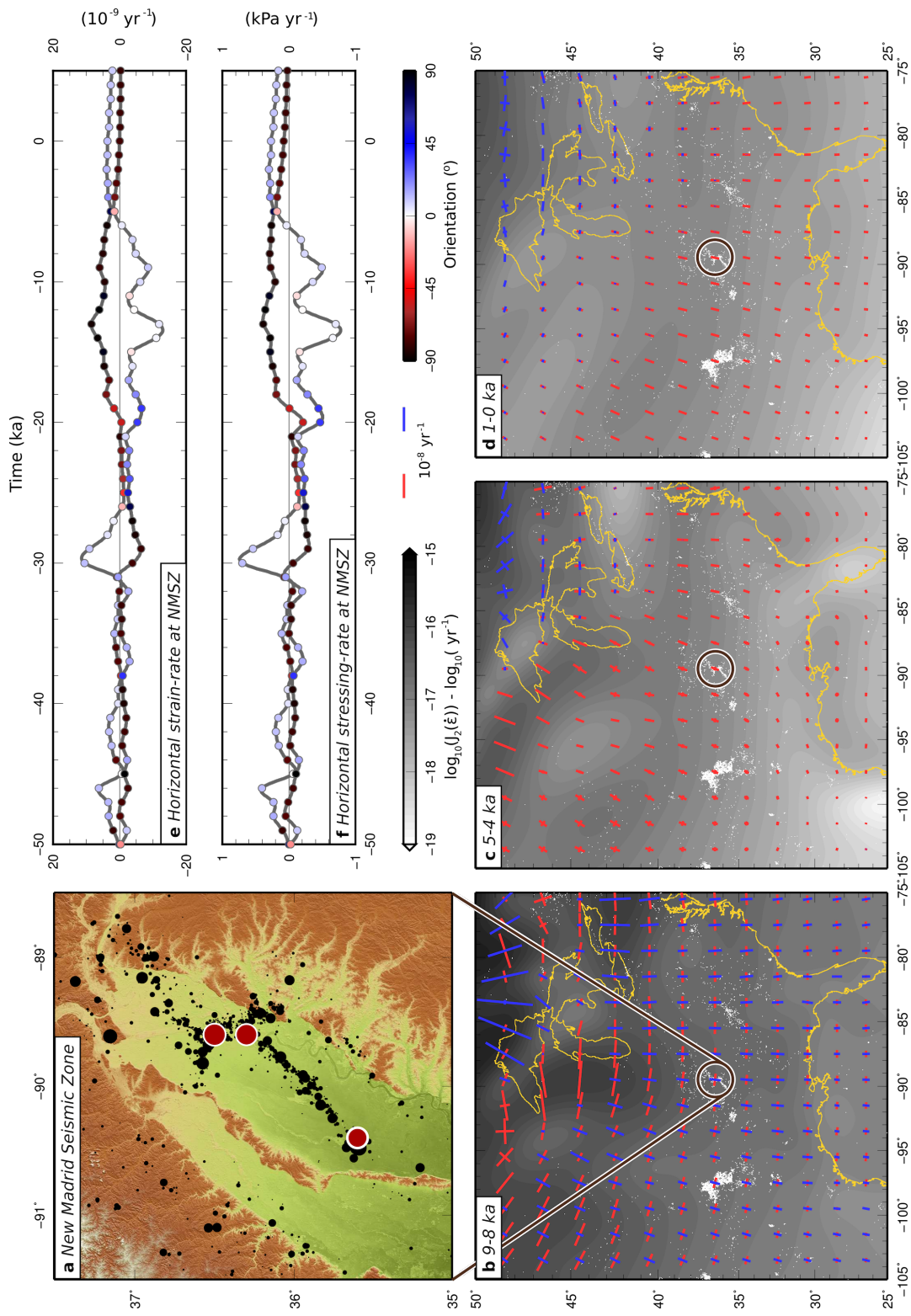


Figure 6: **The New Madrid Seismic Zone.** (a) Seismicity in the New Madrid Seismic Zone, from the CERI catalogue. Red circles are the approximate locations of the 1811–1812 earthquakes. (b) – (d) show the second invariant of the strain-rate tensor (as shading), overlain by principal axes of the strain-rate tensor (blue for extension, red for compression), at three time intervals. (e) shows a time series for the magnitude and (as point colouring) orientation of the principal axes of the strain-rate tensor (expressed as azimuth) at the location of the NMSZ. (f) is as in (e), but for the stressing-rate tensor.

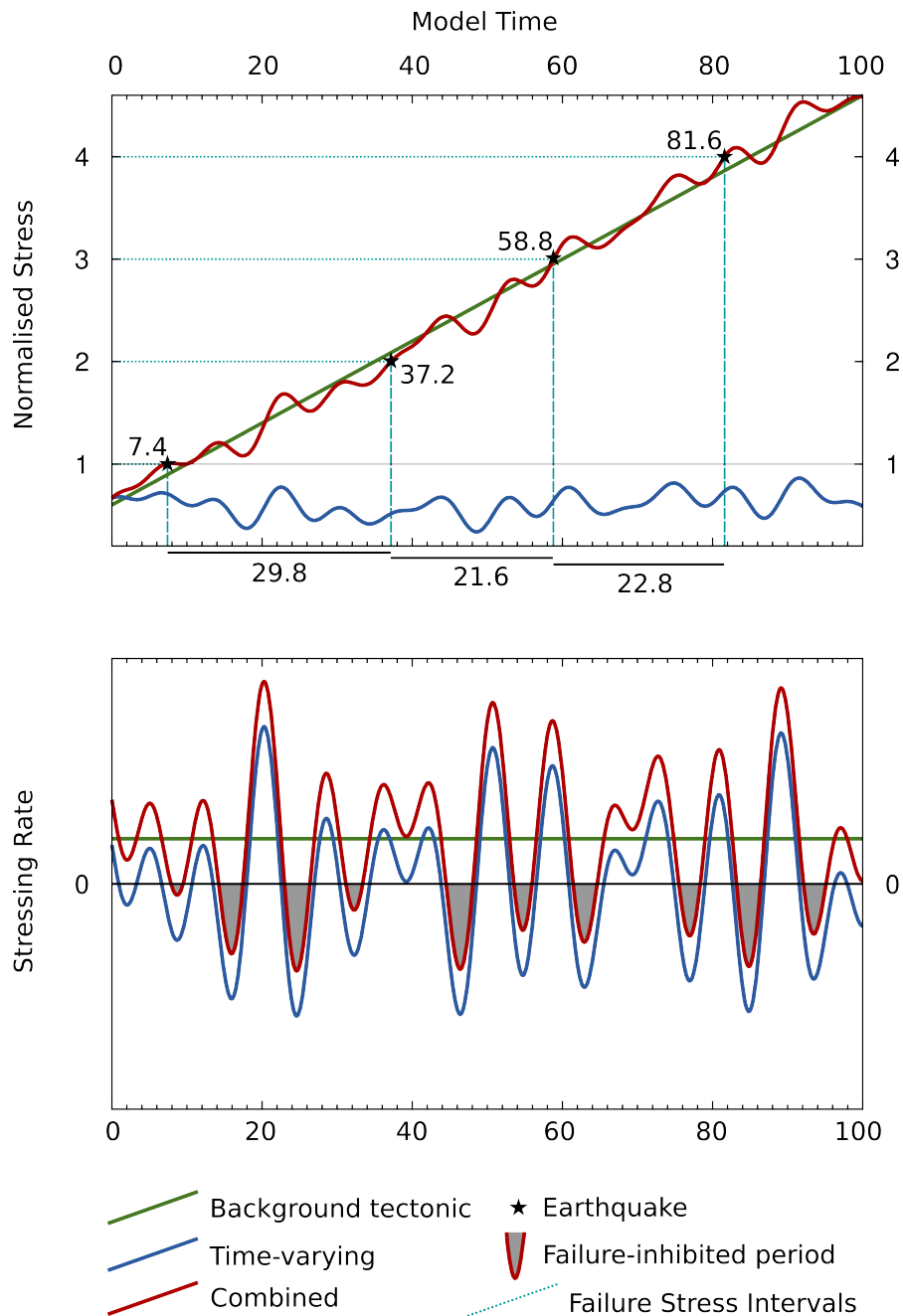


Figure 7: **Schematic stress accumulation in continental interiors.** Simple model for the combination of a uniform background ‘tectonic’ stressing rate, and a superimposed time-variable ‘non-tectonic’ stressing rate. Green indicates the time-invariant tectonic stressing rate, blue the time-variable stressing rate, and red the combined stress as seen by the fault. On the upper panel, turquoise lines indicate earthquakes (shown by black stars), assumed to occur at repeats of the same accumulated total stress, but which occur at variable intervals in model time. On the lower panel, grey-shaded regions indicate time periods where the combined stressing rate is negative, indicating that the fault is unlikely to rupture during these periods, despite the tectonic stress field.